APL Photonics

Efficient photoconductive terahertz detection through photon trapping in plasmonic nanocavities

Cite as: APL Photonics **6**, 080802 (2021); https://doi.org/10.1063/5.0055332
Submitted: 28 April 2021 . Accepted: 28 July 2021 . Published Online: 10 August 2021

N. T. Yardimci, D. Turan, and M. Jarrahi

Efficient photoconductive terahertz detection through photon trapping in plasmonic nanocavities

Cite as: APL Photon. 6, 080802 (2021); doi: 10.1063/5.0055332
Submitted: 28 April 2021 • Accepted: 28 July 2021 •
Published Online: 10 August 2021

N. T. Yardimci,[1,2] D. Turan,[2] and M. Jarrahi[2,a)]

AFFILIATIONS

[1] Lookin, Inc., Los Angeles, California 90066, USA
[2] Electrical and Computer Engineering, University of California, Los Angeles, California 90095, USA

[a)] Author to whom correspondence should be addressed: mjarrahi@ucla.edu

ABSTRACT

We present a photoconductive terahertz detector that employs a plasmonic nanocavity to offer high-sensitivity and broadband operation when used in a terahertz time-domain spectroscopy system even at very low optical pump power levels. By employing a plasmonic nanocavity, all of the photocarriers are generated within a 100 nm distance from the photoconductor contact electrodes, enabling a short transport time for almost all of the photogenerated carriers. As a result, the photoconductive detector maintains high quantum efficiency and ultrafast operation simultaneously, enabling high-sensitivity and broadband operation at very low optical pump power levels. We utilize a photoconductive detector based on a plasmonic nanocavity optimized for operation at a 770 nm optical wavelength in a terahertz time-domain spectroscopy system and demonstrate a 100 dB signal-to-noise ratio and a 0.1–6 THz noise-equivalent bandwidth at a record-low average optical pump power of 0.1 mW, compared to the state-of-the-art photoconductive terahertz detectors. The extremely low optical power budget of the demonstrated photoconductive detector makes this detector attractive for multi-pixel terahertz imaging systems.

I. INTRODUCTION

Terahertz time-domain spectroscopy (THz-TDS) offers unique functionalities for various sensing, hyperspectral imaging, and metrology applications.[1–11] However, the scope and potential use of THz-TDS systems are still limited by the performance of terahertz detectors used in these systems. Photoconductive antennas are the most-preferred type of detectors for THz-TDS systems.[12–24] A conventional photoconductive antenna is fabricated on a short-carrier-lifetime semiconductor, which serves as an ultrafast photoconductor. When the active area of the device is illuminated by a femtosecond optical beam, electron–hole pairs are generated. When a terahertz beam is incident on the photoconductive antenna, a terahertz electric field is induced across the photoconductor contact electrodes, drifting photo-generated carriers and inducing a photocurrent proportional to the incident terahertz field. Thus, by measuring this photocurrent, the temporal and spectral information of the incident terahertz radiation can be obtained.

The amplitude of the terahertz field incident on a photoconductive detector is weak in most applications. Therefore, the induced electric field within the device active area is not large enough for the photo-generated carriers to have high drift velocities. This dramatically limits the number of carriers reaching the contact electrodes before recombining inside the photoconductive substrate. In fact, conventional photoconductive detectors use ~10^{10} incident photons to generate a single electron of the output photocurrent. This limitation in the quantum efficiency has limited the detection sensitivity of the conventional photoconductive detectors.

Various types of metasurfaces and plasmonic structures have been used to increase the responsivity of photoconductive detectors.[25–37] By enhancing optical coupling from air to the photoconductor, photoconductivity and switching contrast increase. However, strong optical absorption does not necessarily lead to a significant enhancement in the terahertz detection sensitivity. The output photocurrent of a photoconductive detector is directly proportional to the number of photo-generated carriers that reach the device contact electrodes within a sub-picosecond time scale.

Therefore, despite the significant increase in the photoconductivity of the demonstrated metasurface-based photoconductive terahertz detectors, their detection sensitivity has been limited because the majority of the photocarriers still recombine in the photoconductor and do not contribute to terahertz detection.

As a solution, we present a large-area photoconductive terahertz detector that employs a plasmonic nanocavity to offer very high optical photon-to-collected electron conversion efficiency. The plasmonic nanocavity is designed to trap almost all of the incident photons inside the photoconductive active region. It is also designed to provide a sub-picosecond transport time for almost all of the photo-generated carriers to the contact electrodes. Consequently, this plasmonic nanocavity offers very high responsivity levels even at very low optical powers with very high switching contrast and terahertz detection sensitivity levels. In addition, the presented detector employs an array of Hertzian dipole nanoantennas to provide a broad terahertz detection bandwidth while operating as the photoconductor contact electrodes. Although a single Hertzian dipole is not an efficient antenna,[38] since the output photocurrent is generated through the cumulative contribution of all of the Hertzian dipole nanoantennas, high responsivity levels are ultimately achieved through the presented photoconductive terahertz detector. It should be noted that similar large-area photoconductor structures have been used as terahertz sources.[39,40] However, the optimum geometries for high-performance terahertz generation and detection are different.

II. DETECTOR DESIGN

The schematic diagram of the presented photoconductive terahertz detector optimized for operation at ~770 nm optical wavelength is shown in Fig. 1. The plasmonic nanocavity is created by embedding a high-mobility photoactive layer between a distributed Bragg reflector (DBR) and the nanoantenna arrays. The structure is designed to trap all of the incident optical photons inside the photoactive layer. The thickness of the photoactive layer (h_{ph}) is kept small to ensure that all of the photogenerated carriers can reach the nanoantenna electrodes in a sub-picosecond time scale when a terahertz pulse is incident on the detector. An anti-reflection dielectric coating is also used to further enhance the optical beam coupling from air to the plasmonic nanocavity. The semiconductor gaps between the adjacent nanoantenna rows are shadowed by another metal layer to prevent inducing a photocurrent in the opposite direction to the output photocurrent of the nanoantennas and to achieve a high dark resistance and switching contrast.

The arrays of Hertzian dipole nanoantennas are designed to offer high responsivity and broadband operation simultaneously. The width (w_{ant}), periodicity (p_{ant}), and metal thickness (h_{Au}) of the nanoantennas are selected to excite surface plasmon waves at the optical pump wavelength so that a strong optical confinement is achieved inside the nanocavity. The length of the nanoantennas (l_{ant}) and the gap between the opposite nanoantenna arrays

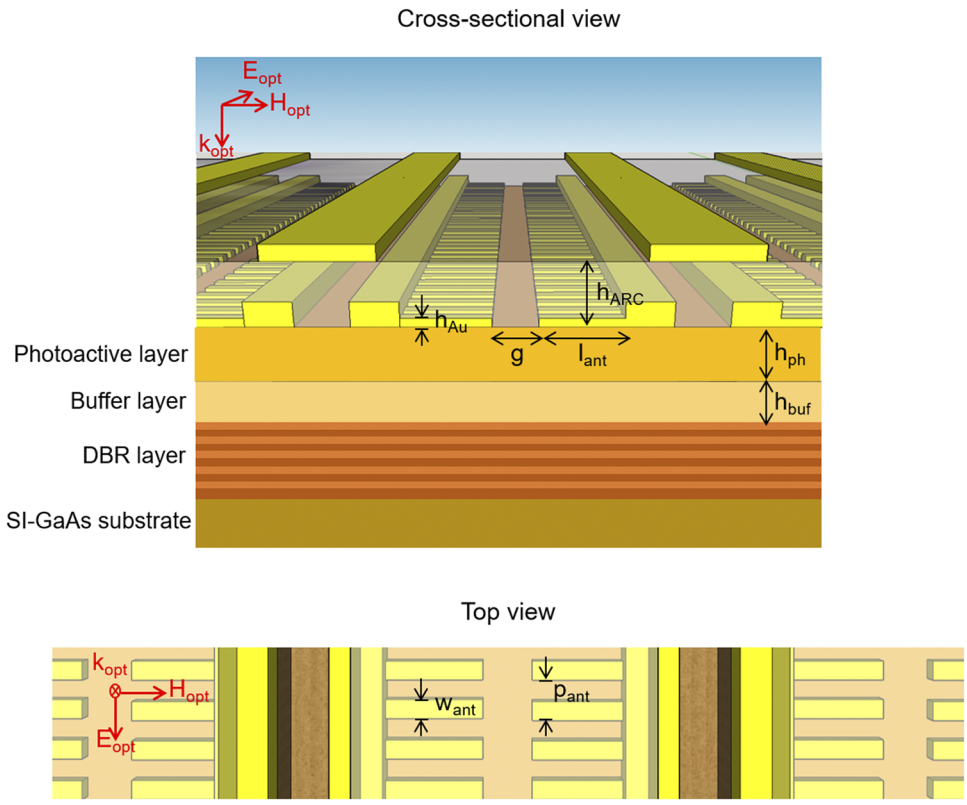

FIG. 1. Schematic diagram of the presented terahertz detector based on a plasmonic nanocavity from the cross-sectional and top views.

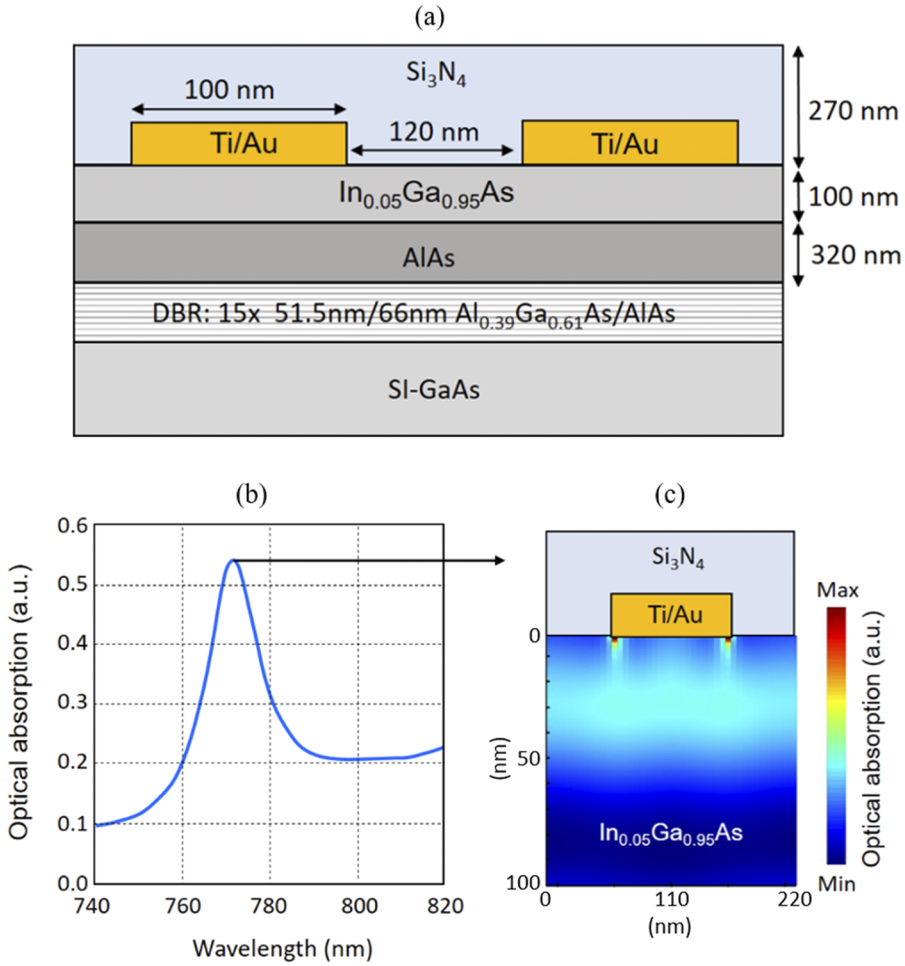

FIG. 2. (a) The cross-sectional view of the optimized nanocavity structure, (b) optical absorption in the $In_{0.05}Ga_{0.95}As$ layer as a function of the optical pump wavelength, and (c) the optical absorption profile in the $In_{0.05}Ga_{0.95}As$ photoactive layer at a 770 nm wavelength.

(g) are selected to maximize the spatial overlap of the photo-generated carrier concentration and the terahertz electric field induced within the photoactive region close to the contact electrodes.[32] As a result, a large fraction of the photo-generated carriers drift to the nanoantennas within a sub-picosecond time scale and a much higher photon-to-collected electron conversion efficiency is achieved compared to the conventional photoconductive terahertz detectors.

The plasmonic nanocavity architecture offers design flexibility in terms of material and geometry selection. This flexibility allows further optimization of the electrical and optical properties of the terahertz detector. By independently controlling the detector resistance and carrier mobility, the responsivity, sensitivity, noise performance, and operation bandwidth of the terahertz detector can be further enhanced.

To achieve a high switching contrast and detection bandwidth, the optical absorption profile is engineered to obtain a strong photoabsorption in close proximity to the contact electrodes, while maintaining a large dark resistance. To maintain a large dark resistance, a very thin photoactive layer with a 100 nm thickness and a 320-nm-thick AlAs buffer layer between the DBR and photoactive layer are used. $In_{0.05}Ga_{0.95}As$ is chosen as the semiconductor for the photoactive layer, instead of the traditionally

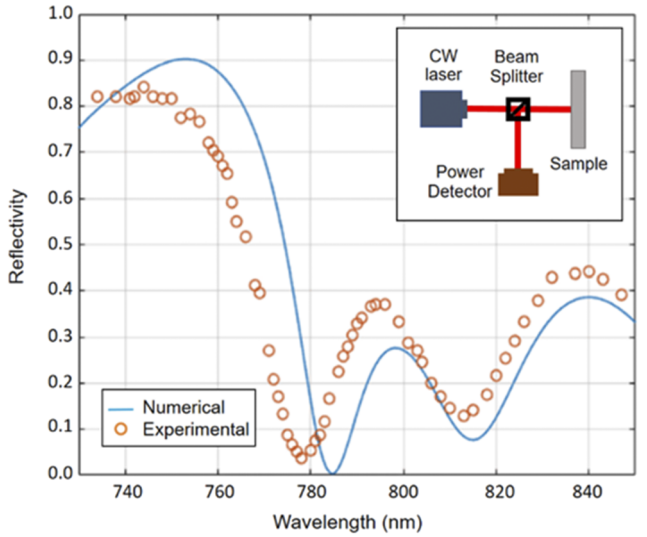

FIG. 3. The measured reflectivity of the grown semiconductor superlattice as a function of optical wavelength and its comparison with the numerical calculations. The experimental setup is illustrated in the inset.

used GaAs, to have higher optical absorption and carrier mobility. Compared to GaAs, $In_{0.05}Ga_{0.95}As$ offers ~13% higher carrier mobility and ~88% higher optical absorption coefficient at 770 nm.

The cross-sectional view of the optimized nanocavity structure is shown in Fig. 2(a). The DBR consists of 15 pairs of 51.5-nm-thick $Al_{0.39}Ga_{0.61}As$ and 66-nm-thick AlAs and is designed to provide high optical reflectivity at ~770 nm wavelength. The geometry of the nanoantennas is selected to excite surface plasmon waves at ~770 nm wavelength when a TM-polarized optical pump beam is incident on the detector.[41] An electromagnetic simulation software program based on the finite-difference time-domain method (Lumerical) is used to analyze the interaction between the optical pump beam and the plasmonic nanoantennas. The simulation results show that the use of plasmonic nanoantennas with a 220 nm periodicity, 100 nm width, and 3/77 nm height Ti/Au with a 270-nm-thick Si_3N_4 anti-reflection coating is expected to provide 53% optical absorption within a 60 nm depth inside the $In_{0.05}Ga_{0.95}As$ photoactive layer below the plasmonic nanoantennas at a 770 nm wavelength, as shown in Figs. 2(b) and 2(c) [~2 times increase in optical absorption compared to low-temperature (LT)-GaAs plasmonic nanoantennas without a nanocavity[32]]. The length of the nanoantennas (4 μm) and the gap between the opposite nanoantennas (0.5 μm) are selected to maximize the spatial overlap between the terahertz and optical fields.[32]

III. DETECTOR FABRICATION AND CHARACTERIZATION RESULTS

After the completion of the detector design, the semiconductor superlattice is grown through molecular beam epitaxy (MBE).

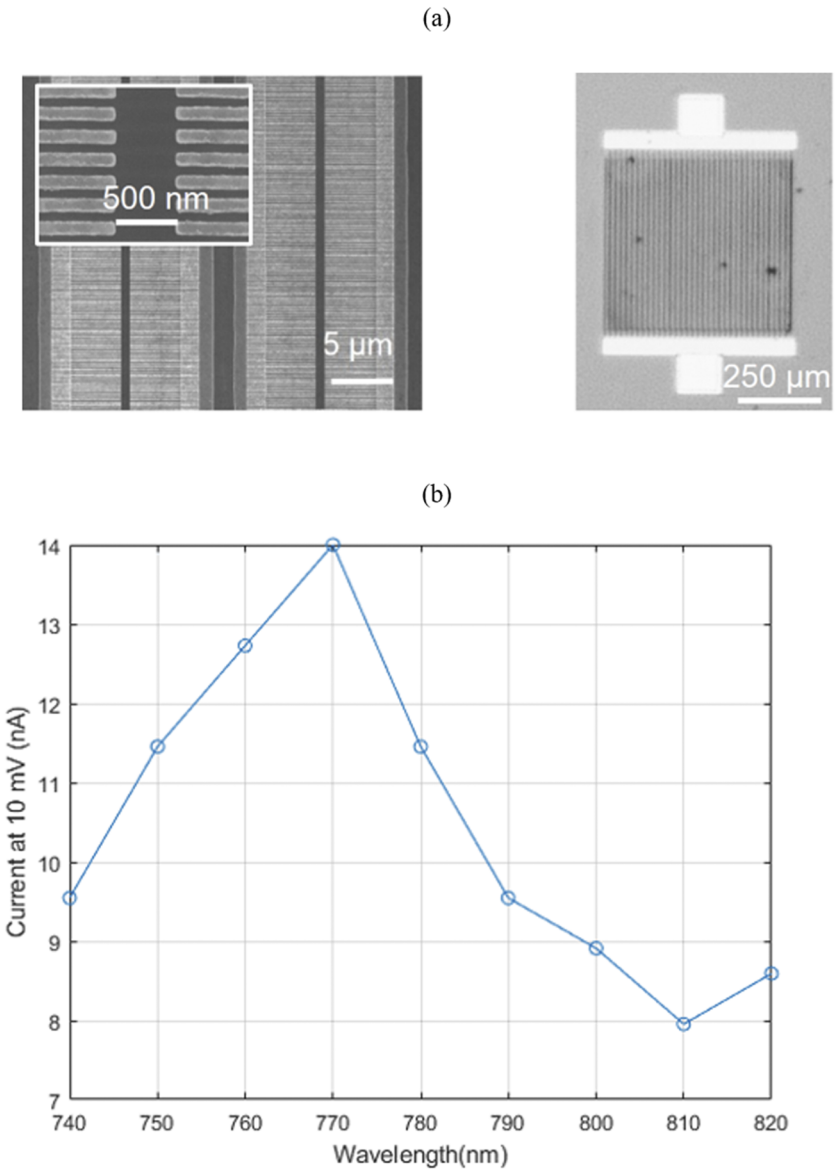

FIG. 4. (a) Optical and scanning electron microscopy images of the fabricated detector. (b) The measured photocurrent at an average optical power of 0.1 mW, as a function of optical wavelength.

The AlAs/AlGaAs DBR, AlAs buffer, and $In_{0.05}Ga_{0.95}As$ photoactive layers are grown on a semi-insulating GaAs (SI-GaAs) substrate. The characterization of the molecular composition and thickness is performed using x-ray diffraction (XRD), which verifies the growth quality and accuracy. According to the XRD results, the grown structure is 15 × 51.5/66 nm $Al_{0.39}Ga_{0.61}As$/AlAs + 320 nm AlAs + 98 nm $In_{0.05}Ga_{0.95}As$, showing only a deviation of 2 nm from the targeted 100 nm thickness of the photoactive layer. To verify the photon trapping performance of the grown semiconductor superlattice before the nanoantenna fabrication, the reflectance of the grown semiconductor is measured under a normal optical incidence. For this purpose, a tunable continuous-wave (CW) Ti:sapphire laser (Coherent Mira HP) is used. The schematic of the experimental setup is shown in the inset of Fig. 3. A beam splitter is used to route the reflected light from the surface of the sample to an optical power detector. A low optical power level (1 mW) is applied to prevent any secondary effects, such as saturation or bleaching. Figure 3 shows the reflectivity of the semiconductor superlattice as a function of wavelength and its comparison with the numerical predictions calculated using Lumerical, indicating a close agreement with the numerical predictions. The 6 nm blue shift from the numerical predictions is due to the small deviation in the thickness of the photoactive $In_{0.05}Ga_{0.95}As$ layer.

A detector prototype with a 100 × 100 μm^2 area is fabricated on the grown semiconductor superlattice. The first step of the fabrication process is electron-beam (e-beam) lithography to pattern the plasmonic nanoantennas. This process is followed by a 3/77 nm Ti/Au deposition through metal evaporation and lift-off. Next, the current collector lines are patterned through optical lithography, which is followed by a 10/100 nm Ti/Au metal deposition and lift-off. The contact vias are deposited using another optical lithography step, 20/200 nm Ti/Au deposition, and lift-off. The 270-nm-thick

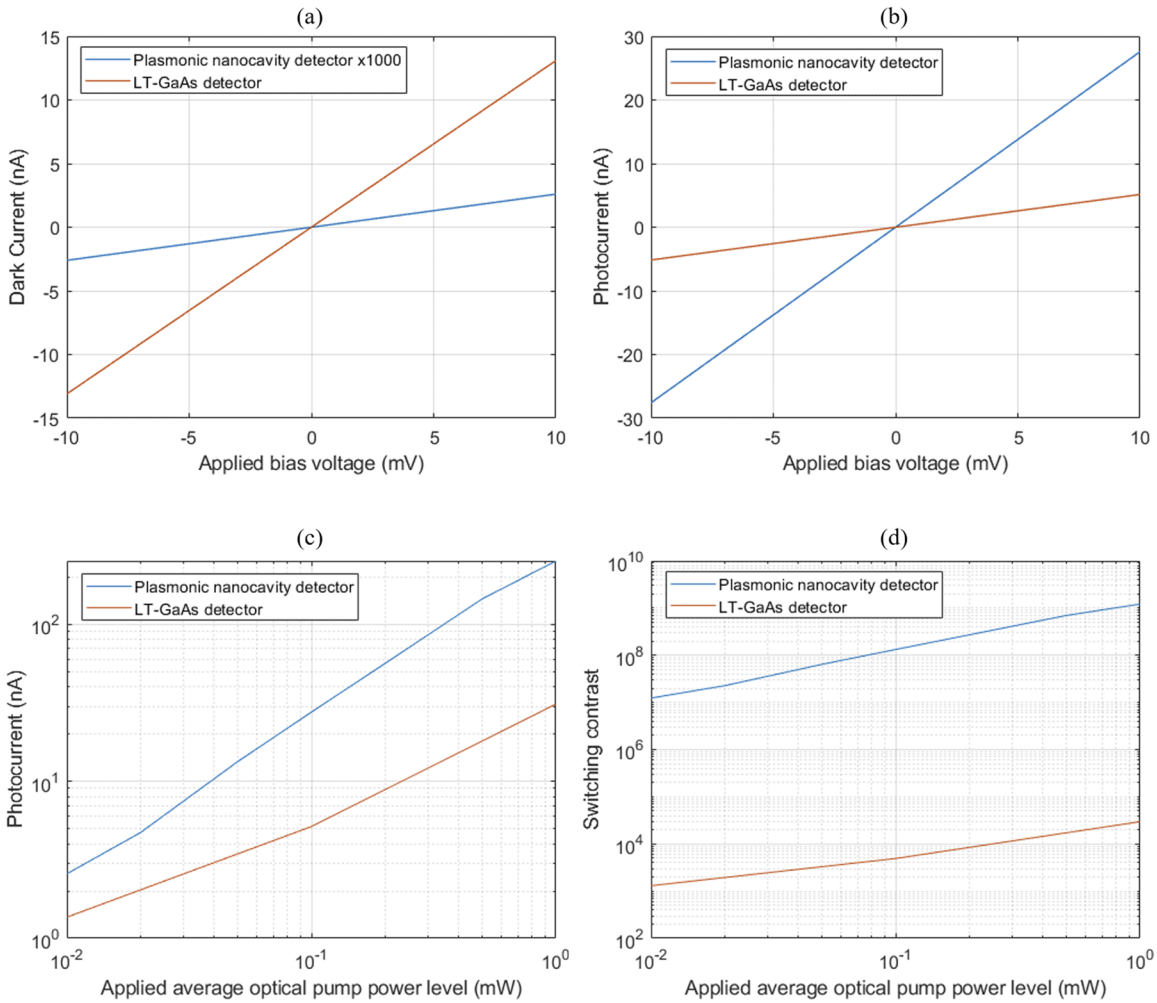

FIG. 5. (a) The dark current levels of the plasmonic nanocavity detector and the LT-GaAs detector as a function of the bias voltage (the dark current of the plasmonic nanocavity detector is multiplied by 1000 to be in the same order-of-magnitude as the LT-GaAs detector), (b) the photocurrent levels at an average optical power of 0.1 mW as a function of the bias voltage, (c) the photocurrent levels as a function of the optical pump power level at a 10 mV bias voltage, and (d) the switching contrast of the detectors as a function of the optical pump power level.

Si_3N_4 anti-reflection coating is deposited through plasma-enhanced chemical vapor deposition (PECVD). Another optical lithography step is used to pattern the contact vias, which is followed by a Si_3N_4 etching step to open the contact pads. Finally, the shadow metals are deposited through another optical lithography step followed by 10/100 nm Ti/Au deposition and lift-off. The optical and scanning electron microscopy (SEM) images of the fabricated detector are shown in Fig. 4(a). The fabricated detector is mounted on a hemispherical silicon lens with a 12 mm diameter and placed on a manual rotation mount for characterization.

Figure 4(b) shows the measured photocurrent from the detector at a bias voltage of 10 mV and an average optical power of 0.1 mW, as a function of the optical wavelength, indicating a significant optical absorption enhancement at a 770 nm wavelength as expected from the theoretical predictions.

To better demonstrate the performance enhancement offered by the presented plasmonic nanocavity detector, the performance of the fabricated detector is compared with a photoconductive detector based on a plasmonic nanoantenna array fabricated on a low-temperature (LT) grown GaAs substrate, which has provided record-high signal-to-noise ratio (SNR) levels when used in THz-TDS systems.[32] The dark IV characteristics of both detectors are shown in Fig. 5(a), indicating that the plasmonic nanocavity detector has more than 3 orders of magnitude larger dark resistance than the LT-GaAs detector. The higher dark resistance of the plasmonic nanocavity detector is directly translated to a higher switching contrast.[42] The detector photocurrent levels are measured using a femtosecond laser (Toptica FemtoFiber Smart780) that produces 80 fs pulses with an 80 MHz repetition rate. Comparing the photocurrent levels of the two detectors shows a

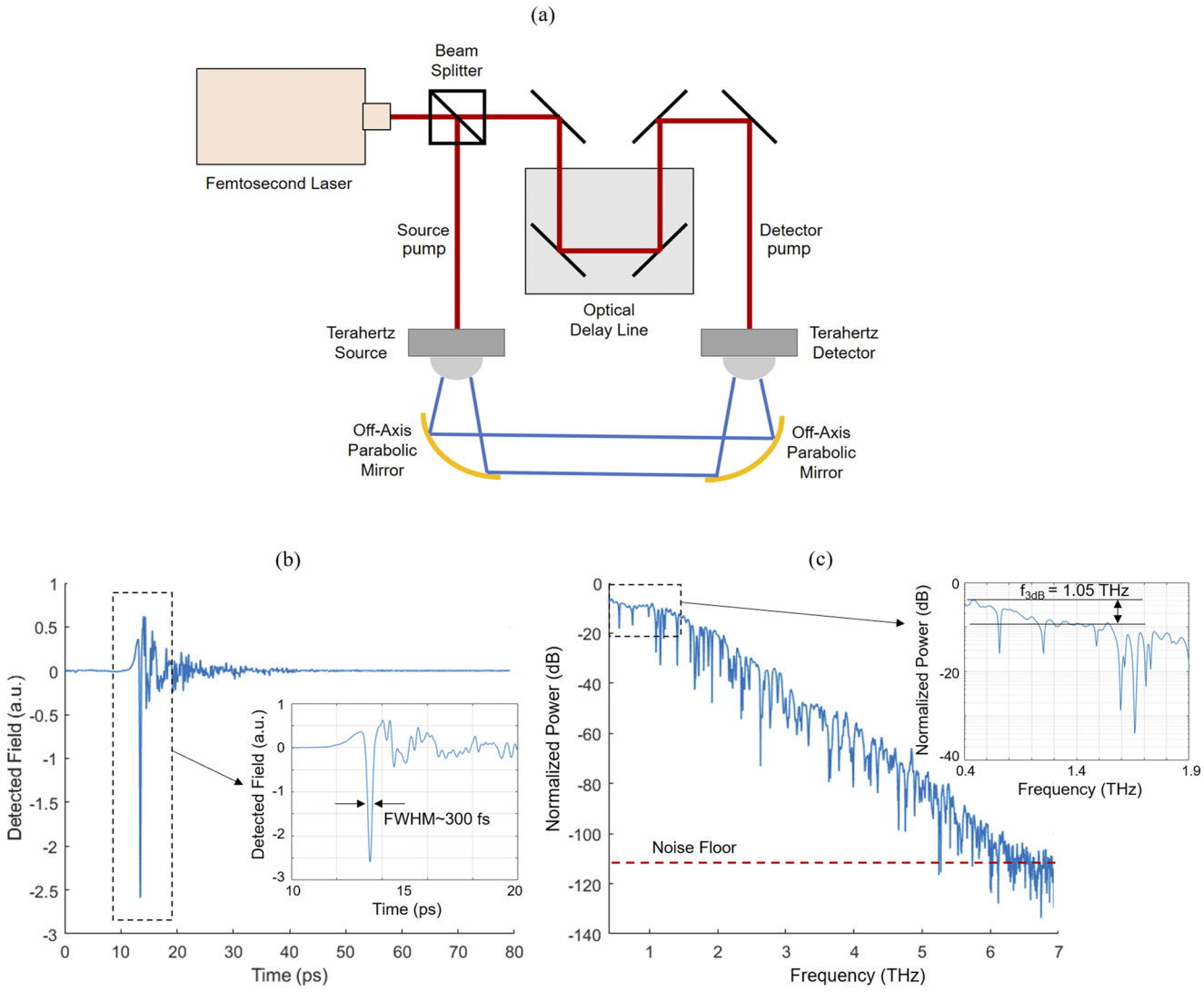

FIG. 6. (a) The schematic diagram of the THz-TDS setup. (b) The detected time-domain terahertz field and (c) the corresponding power spectrum of the detected terahertz signal. The noise level is calculated by taking the average of the resolved power between 7 and 10 THz.

significant enhancement in the detected photocurrent by the plasmonic nanocavity detector [Fig. 5(b)]. This enhancement indicates the stronger responsivity of the plasmonic nanocavity detector due to the very strong optical absorption within the photoactive layer as well as the higher carrier mobility of the low-defect $In_{0.05}Ga_{0.95}As$ photoactive layer. The comparison between the average photocurrent of the two detectors at a 10 mV bias voltage as a function of the optical pump power is shown in Fig. 5(c), also proving the superior responsivity and quantum efficiency of the plasmonic nanocavity detector.

The switching contrast of the detectors, defined as the ratio of the OFF state resistance (in the absence of optical excitation) to the ON state resistance (in the presence of optical excitation), is calculated as $\frac{I_{ph}}{I_{dark} * t_{exc} * f_{rep}}$, where I_{ph} is the average photocurrent, I_{dark} is the dark current, t_{exc} is the photo-excitation time (i.e., the pulse width of the femtosecond pulses), and f_{rep} is the repetition rate of the laser. The switching contrast of each detector as a function of the optical pump wavelength is shown in Fig. 5(d). Because of the larger dark resistance and quantum efficiency of the plasmonic nanocavity detector, this detector offers more than 4 orders of magnitude larger switching contrast compared to the LT-GaAs detector.

Terahertz detection performance of the plasmonic nanocavity detector is characterized using a THz-TDS setup [Fig. 6(a)]. Femtosecond optical pulses are split into two parts by using a beam splitter pellicle. One part is focused on a terahertz source based on plasmonic nanoantenna arrays.[40] The terahertz source generates terahertz pulses, and the radiation is focused on the terahertz detector. The other part of the optical beam is also focused on the terahertz detector. An optical delay line is used to change the delay between the terahertz and optical pulses incident on the terahertz detector. Hence, the generated photocurrent due to the terahertz radiation is sampled. The generated photocurrent is amplified using a transimpedance amplifier (Femto DHPCA-200) with a gain of 10^6 V/A, then routed to a lock-in amplifier (Zurich Instruments MFLI) for data acquisition. The bias voltage of the terahertz source, and thus the terahertz radiation power, is modulated with a 100 kHz sinusoidal wave through the internal oscillator of the lock-in amplifier.

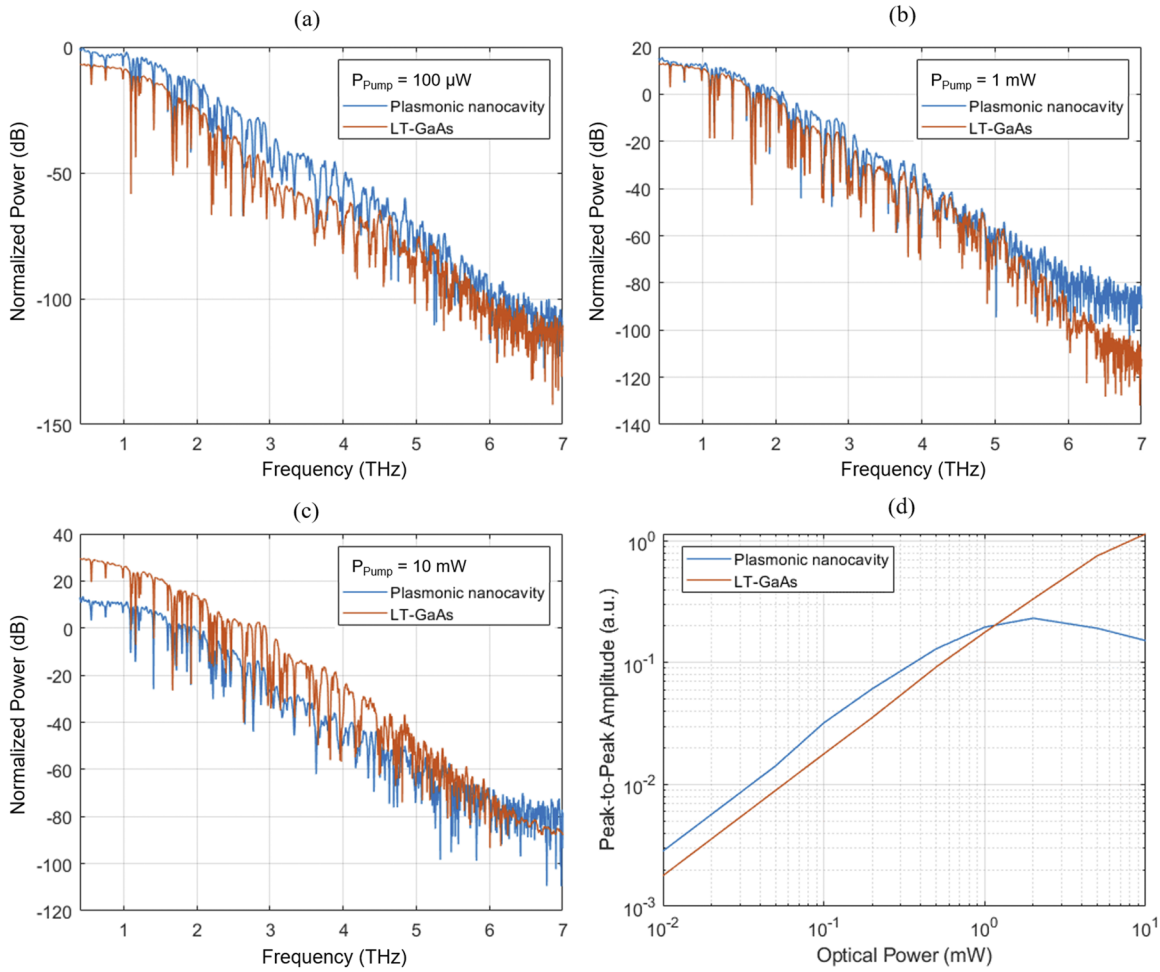

FIG. 7. The detected spectra by the plasmonic nanocavity and LT-GaAs detectors at (a) 100 μW, (b) 1 mW, and (c) 10 mW optical pump power levels. (d) The peak-to-peak terahertz field calculated from the time-domain signals obtained at different optical power levels.

This signal is also used as the reference signal for lock-in operation. For each measurement, the terahertz traces are acquired for 1 s, during which 4 THz pulse traces are captured. The acquired traces are averaged, and the final terahertz pulse trace for each measurement is obtained.

Figure 6(b) shows the time-domain signal obtained under a 100 μW optical pump power level. The full-width at half-maximum of the terahertz pulse is measured to be ~300 fs. The corresponding power spectrum of the detected terahertz pulse is calculated by taking the Fourier transform of the time-domain signal. The frequency-domain signal is shown in Fig. 6(c). With only a 1 s measurement (4 averages), an ~100 dB dynamic range and a 6 THz detection bandwidth are achieved. The 3-dB bandwidth of the detector is measured to be 1.05 THz.

To compare the terahertz detection performance of the plasmonic nanocavity detector and the LT-GaAs detector, the terahertz pulses from both detectors are acquired at different optical pump power levels. Figures 7(a)–7(c) show the frequency-domain output signals detected by both detectors at 100 μW, 1 mW, and 10 mW optical pump power levels, respectively. At 100 μW, the plasmonic nanocavity detector offers superior performance compared to the LT-GaAs detector. Since the photocarrier concentration is much higher in the active region of the plasmonic nanocavity detector, at larger optical power levels, the LT-GaAs detector starts offering larger dynamic range and bandwidth values. To better understand the effect of the optical pump power on the detector performance, the peak-to-peak amplitude of the time-domain field detected by both detectors is calculated as a function of the optical pump power level. The peak-to-peak amplitude is directly proportional to the responsivity of the terahertz detectors. In the absence of any saturation or carrier screening effect, the detector responsivity should increase linearly as the optical pump power level increases because the photocurrent level is directly proportional to the photocarrier concentration. However, due to the strong light confinement in the plasmonic nanocavity detector, the responsivity of this detector starts to drop above 2 mW due to carrier screening, as it can be seen in Fig. 7(d). On the other hand, the LT-GaAs detector does not suffer from carrier screening at these optical power levels due to the short lifetime of the carriers in the LT-GaAs substrate.

IV. CONCLUSION

In summary, we developed an extremely efficient photoconductive terahertz detector that offers a very large SNR and detection bandwidth at record-low optical pump power levels. This detector is realized using a plasmonic nanocavity that confines the optical pump photons very tightly in a thin photoactive layer. The plasmonic nanocavity is comprised of a DBR and an array of plasmonic nanoantennas. The photoactive region is placed right under the plasmonic nanoantennas so that the photogenerated carriers can quickly drift to the nanoantennas in a sub-picosecond time scale, ensuring an ultrafast operation. By enhancing the quantum efficiency while maintaining an ultrafast operation, very high responsivity levels are achieved even at very low optical power levels. This high-efficiency performance is experimentally demonstrated and it is shown that a THz-TDS system employing the plasmonic nanocavity detector can offer more than a 100 dB SNR and a 6 THz noise-equivalent bandwidth at a record-low average optical pump power of 0.1 mW with only a 1-s measurement. The experimental results also show that the presented detector offers very large switching contrasts, above 10^8 at a 0.1 mW average optical pump power level, which are 4-orders of magnitude higher than the state-of-the-art photoconductive terahertz detectors. Depending on the application requirements, the presented detector can be operated at other optical pump power levels with different measurement times. For example, even lower optical pump powers can be used for low-power-budget applications, resulting in a quadratic drop in the SNR as a function of the optical pump power and reduction in bandwidth. Longer measurement and integration times can boost the SNR with a linear increase in the SNR as a function of the measurement time. For example, the presented detector offers an SNR of 74 dB and a 5 THz noise-equivalent bandwidth at optical pump powers as low as 63 nW with a 6250-s measurement, exhibiting an order-of-magnitude enhancement in SNR compared to broadband plasmonic terahertz field detectors utilizing nonlinear mixing processes at exactly the same optical pump power and measurement time.[43] The extremely low optical power budget of the demonstrated photoconductive detector makes this detector attractive for multi-pixel terahertz imaging systems.[44] Furthermore, providing ultrashort transport times for the majority of the photogenerated carriers eliminates the necessity of using short-carrier-lifetime substrates. This unprecedented capability has a tremendous impact on future THz-TDS systems. It would enable the utilization of new materials and/or new lasers operating at various optical wavelengths, which were not possible before due to the lack of short carrier lifetime photo-absorbing semiconductors with acceptable dark resistance and carrier mobility.

AUTHORS' CONTRIBUTIONS

All authors contributed to the design of the plasmonic nanocavity and terahertz detector. N.T.Y. fabricated and characterized the terahertz detectors. N.T.Y. and M.J. prepared the manuscript.

ACKNOWLEDGMENTS

The authors acknowledge the financial support from the Burroughs Wellcome Fund. N.T.Y. was supported by the US Department of Energy (Award No. DE-SC0020521). D.T. was supported by the US Department of Energy (Award No. DE-SC0016925).

N.T.Y. and M.J. declare competing financial interest.

DATA AVAILABILITY

The data that support the findings of this study are available from the corresponding author upon reasonable request.

REFERENCES

[1] B. B. Hu and M. C. Nuss, Opt. Lett. **20**, 1716 (1995).
[2] D. M. Mittleman, R. H. Jacobsen, and M. C. Nuss, IEEE J. Sel. Top. Quantum Electron. **2**, 679 (1996).
[3] M. Tonouchi, Nat. Photonics **1**, 97 (2007).
[4] D. Graham-Rowe, Nat. Photonics **1**, 75 (2007).
[5] D. M. Mittleman, Opt. Express **26**, 9417 (2018).
[6] J. A. Zeitler, P. F. Taday, D. A. Newnham, M. Pepper, K. C. Gordon, and T. Rades, J. Pharm. Pharmacol. **59**, 209 (2007).

[7]M. Scheller, C. Jansen, and M. Koch, Opt. Commun. **282**, 1304 (2009).
[8]A. A. Gowen, C. O'Sullivan, and C. P. O'Donnell, Trends Food Sci. Technol. **25**, 40 (2012).
[9]Q. Sun, Y. He, K. Liu, S. Fan, E. P. J. Parrott, and E. Pickwell-MacPherson, Quant. Imaging Med. Surg. **7**, 345 (2017).
[10]M. Browne, N. T. Yardimci, C. Scoffoni, M. Jarrahi, and L. Sack, Plant Direct **4**, e00197 (2020).
[11]C. L. Koch-Dandolo, T. Filtenborg, K. Fukunaga, J. Skou-Hansen, and P. U. Jepsen, Appl. Opt. **54**, 5123 (2015).
[12]P. R. Smith, D. H. Auston, and M. C. Nuss, IEEE J. Quantum Electron. **24**, 255 (1988).
[13]F. G. Sun, G. A. Wagoner, and X. C. Zhang, Appl. Phys. Lett. **67**, 1656 (1995).
[14]M. Tani, K.-S. Lee, and X.-C. Zhang, Appl. Phys. Lett. **77**, 1396 (2000).
[15]S. Kono, M. Tani, P. Gu, and K. Sakai, Appl. Phys. Lett. **77**, 4104 (2000).
[16]T.-A. Liu, M. Tani, M. Nakajima, M. Hangyo, and C.-L. Pan, Appl. Phys. Lett. **83**, 1322 (2003).
[17]E. Castro-Camus, J. Lloyd-Hughes, M. B. Johnston, M. D. Fraser, H. H. Tan, and C. Jagadish, Appl. Phys. Lett. **86**, 254102 (2005).
[18]M. Suzuki and M. Tonouchi, Appl. Phys. Lett. **86**, 163504 (2005).
[19]F. J. O'Hara, J. M. O. Zide, A. C. Gossard, A. J. Taylor, and R. D. Averitt, Appl. Phys. Lett. **88**, 251119 (2006).
[20]F. Peter, S. Winnerl, S. Nitsche, A. Dreyhaupt, H. Schneider, and M. Helm, Appl. Phys. Lett. **91**, 081109 (2007).
[21]K. Peng, P. Parkinson, L. Fu, Q. Gao, N. Jiang, Y.-N. Guo, F. Wang, H. J. Joyce, J. L. Boland, H. H. Tan, C. Jagadish, and M. B. Johnston, Nano Lett. **15**, 206 (2015).
[22]R. J. B. Dietz, A. Brahm, A. Velauthapillai, A. Wilms, C. Lammers, B. Globisch, M. Koch, G. Notni, A. Tünnermann, T. Göbel, and M. Schell, J. Infrared, Millimeter, Terahertz Waves **36**, 60 (2015).
[23]B. Globisch, R. J. B. Dietz, S. Nellen, T. Göbel, and M. Schell, AIP Adv. **6**, 125011 (2016).
[24]R. B. Kohlhaas, S. Breuer, S. Nellen, L. Liebermeister, M. Schell, M. P. Semtsiv, W. T. Masselink, and B. Globisch, Appl. Phys. Lett. **114**, 221103 (2019).
[25]P.-K. Lu, D. Turan, and M. Jarrahi, Opt. Express **28**, 26324 (2020).
[26]D. Turan, N. T. Yardimci, and M. Jarrahi, Opt. Express **28**, 3835 (2020).
[27]N. Wang, S. Cakmakyapan, Y.-J. Lin, H. Javadi, and M. Jarrahi, Nat. Astron. **3**, 977 (2019).
[28]T. Siday, P. P. Vabishchevich, L. Hale, C. T. Harris, T. S. Luk, J. L. Reno, I. Brener, and O. Mitrofanov, Nano Lett. **19**, 2888 (2019).
[29]N. T. Yardimci, D. Turan, S. Cakmakyapan, and M. Jarrahi, Appl. Phys. Lett. **113**, 251102 (2018).
[30]N. T. Yardimci and M. Jarrahi, Small **14**, 1802437 (2018).
[31]O. Mitrofanov, T. Siday, R. J. Thompson, T. S. Luk, I. Brener, and J. L. Reno, APL Photonics **3**, 051703 (2018).
[32]N. T. Yardimci and M. Jarrahi, Sci. Rep. **7**, 42667 (2017).
[33]M. Jarrahi, IEEE Trans. Terahertz Sci. Technol. **5**, 391 (2015).
[34]O. Mitrofanov, I. Brener, T. S. Luk, and J. L. Reno, ACS Photonics **2**, 1763 (2015).
[35]C. W. Berry, N. Wang, M. R. Hashemi, M. Unlu, and M. Jarrahi, Nat. Commun. **4**, 1622 (2013).
[36]B. Heshmat, H. Pahlevaninezhad, Y. Pang, M. Masnadi-Shirazi, R. Burton Lewis, T. Tiedje, R. Gordon, and T. E. Darcie, Nano Lett. **12**, 6255 (2012).
[37]S. Liu, X. Shou, and A. Nahata, IEEE Trans. Terahertz Sci. Technol. **1**, 412 (2011).
[38]C. Balanis, *Antenna Theory: Analysis and Design* (John Wiley & Sons, Inc., 2015).
[39]P. J. Hale, J. Madeo, C. Chin, S. S. Dhillon, J. Mangeney, J. Tignon, and K. M. Dani, Opt. Express **22**, 26358 (2014).
[40]N. T. Yardimci, S.-H. Yang, C. W. Berry, and M. Jarrahi, IEEE Trans. Terahertz Sci. Technol. **5**, 223 (2015).
[41]B.-Y. Hsieh and M. Jarrahi, J. Appl. Phys. **109**, 084326 (2011).
[42]N. Wang and M. Jarrahi, J. Infrared, Millimeter, Terahertz Waves **34**, 519 (2013).
[43]Y. Salamin, I. C. Benea-Chelmus, Y. Fedoryshyn, W. Heni, D. L. Elder, L. R. Dalton, J. Faist, and J. Leuthold, Nat. Commun. **10**, 5550 (2019).
[44]A. Brahm, A. Wilms, R. J. B. Dietz, T. Göbel, M. Schell, G. Notni, and A. Tünnermann, Opt. Express **22**, 12982 (2014).